Research Article

ADVANCED PHOTONICS

Simultaneous ultraviolet, visible, and near-infrared continuous-wave lasing in a rare-earth-doped microcavity

Bo Jiang,[a] Song Zhu,[a,b] Linhao Ren,[a] Lei Shi,[a,c,]* and Xinliang Zhang[a,c]
[a]Huazhong University of Science and Technology, Wuhan National Laboratory for Optoelectronics, Wuhan, China
[b]Nanyang Technological University, School of Electrical and Electronic Engineering, Singapore
[c]Optics Valley Laboratory, Wuhan, China

Abstract. Microlaser with multiple lasing bands is critical in various applications, such as full-color display, optical communications, and computing. Here, we propose a simple and efficient method for homogeneously doping rare earth elements into a silica whispering-gallery microcavity. By this method, an Er-Yb co-doped silica microsphere cavity with the highest quality (Q) factor (exceeding 10^8) among the rare-earth-doped microcavities is fabricated to demonstrate simultaneous and stable lasing covering ultraviolet, visible, and near-infrared bands under room temperature and a continuous-wave pump. The thresholds of all the lasing bands are estimated to be at the submilliwatt level, where both the ultraviolet and violet continuous wave upconversion lasing from rare earth elements has not been separately demonstrated under room temperature until this work. This ultrahigh-Q doped microcavity is an excellent platform for high-performance multiband microlasers, ultrahigh-precision sensors, optical memories, and cavity-enhanced light–matter interaction studies.

Keywords: multiband microlasers; whispering-gallery microcavities; rare earth elements; upconversion.

Received Nov. 24, 2021; revised manuscript received Apr. 28, 2022; accepted for publication Jun. 14, 2022; published online Jul. 9, 2022.

[DOI: 10.1117/1.AP.4.4.046003]

1 Introduction

Multiband lasers are attractive for their potential applications in color display, lighting, wavelength-division multiplexing, optical communications, and computing.[1–4] Rare earth (RE) elements with abundant long-lived intermediate energy levels and intraconfigurational transitions can emit light from the deep-ultraviolet to mid-infrared by pumping high-energy or low-energy photons, i.e., downshifting or upconversion, respectively, and thus can be applied in data storage,[5,6] three-dimensional display,[7,8] luminescent biomarkers,[9–11] and lasers.[12,13] Whispering-gallery-mode (WGM) optical microcavities with an ultrahigh quality (Q) factor and small mode volume exhibiting ultrahigh energy density and strong light–matter interaction can be applied in sensing,[14–16] nonlinear optics,[17–22] cavity optomechanics,[23,24] and lasers.[25–33] Therefore, doping RE elements into an ultrahigh-Q microcavity without degrading its intrinsic Q factor is an effective way to construct a low-threshold and narrow-linewidth multiband microlaser.

By implanting erbium (Er) ions into a microdisk cavity under 2 MeV acceleration, Kippenberg et al.[30] realized a microlaser in the 1550-nm band with a threshold as low as 43 μW for a resonant pump. Yang et al.[31] processed a sol–gel-based Er-silica film to form a doped microtoroid cavity, achieving the lowest lasing threshold of 660 nW in the 1550-nm band under a resonant pump. Besides the luminescence in the 1550-nm band, the upconversion luminescence by Er ions also attracts great interest. Based on the sol–gel technology, Lu et al.[34] fabricated a highly Er-doped microtoroid cavity with a Q factor of 10^7, realizing a green upconversion laser with a threshold of 690 μW for a resonant pump. Recently, Bravo et al.[35] achieved a CW red laser from an Er-upconverting-nanoparticle-coated plasmon cavity with a threshold of 70 $\mathrm{W/cm^2}$. Zhu et al.[36] employed $\mathrm{NaYF_4:Yb/Er@NaYF_4}$ core-shell upconversion nanocrystals

---

*Address all correspondence to Lei Shi, lshi@hust.edu.cn as the gain material, realizing simultaneous lasing in the 410-, 540-, and 655-nm bands by a bottle-like WGM microcavity under a 3-pulse pump system. Spontaneous upconversion emission of RE elements has been widely investigated from the deep-ultraviolet to the near-infrared. However, to the best of our knowledge, under room temperature and CW pump, stimulated ultraviolet and violet upconversion emissions have not been separately reported. The main reason should be that the inhomogeneity of a doped cavity will cause an extremely large scattering loss in the short-wavelength band. Therefore, a doped cavity with an ultrahigh Q factor should be the key to achieving short-wavelength lasing.

In this work, we introduce polymethyl methacrylate for doping RE ions homogeneously. Consequently, an ultrahigh-Q ($Q_{\text{loaded}} = 1.2 \times 10^8$ in the telecommunications band) Er-Yb co-doped silica microsphere cavity is fabricated, achieving simultaneous CW lasing in the ultraviolet, visible, and near-infrared bands at room temperature for the first time to our knowledge. The lasing thresholds under a nonresonant pump are estimated to be 480, 170, 2.7, 18, 0.18, 1.7, 10, and 38 μW for the 380-, 410-, 450-, 560-, 660-, 800-, 1080-, and 1550-nm bands, respectively, of which the ultraviolet and violet CW lasing by RE elements has not been separately demonstrated under a room temperature pump until this work. The Er-Yb co-doped microsphere also shows a great lasing stability over 190 min, indicating a stable and high-performance multiband laser source for practical applications.

2 Device Characterization and Experiment Setup

The design and fabrication details of an Er-Yb co-doped microsphere cavity are described in Sec. S1 in the Supplementary Material. As shown in Fig. 1(a), the Er-Yb co-doped microsphere cavity with a diameter of about 57 μm is coupled via an optical microfiber with a diameter of about 1.2 μm. The microsphere cavity is pumped by a 975-nm CW semiconductor laser with a linewidth of 1 nm, producing simultaneous ultraviolet, visible, and near-infrared CW lasing. In this pump scheme, the pump laser with the linewidth of 1 nm can cover

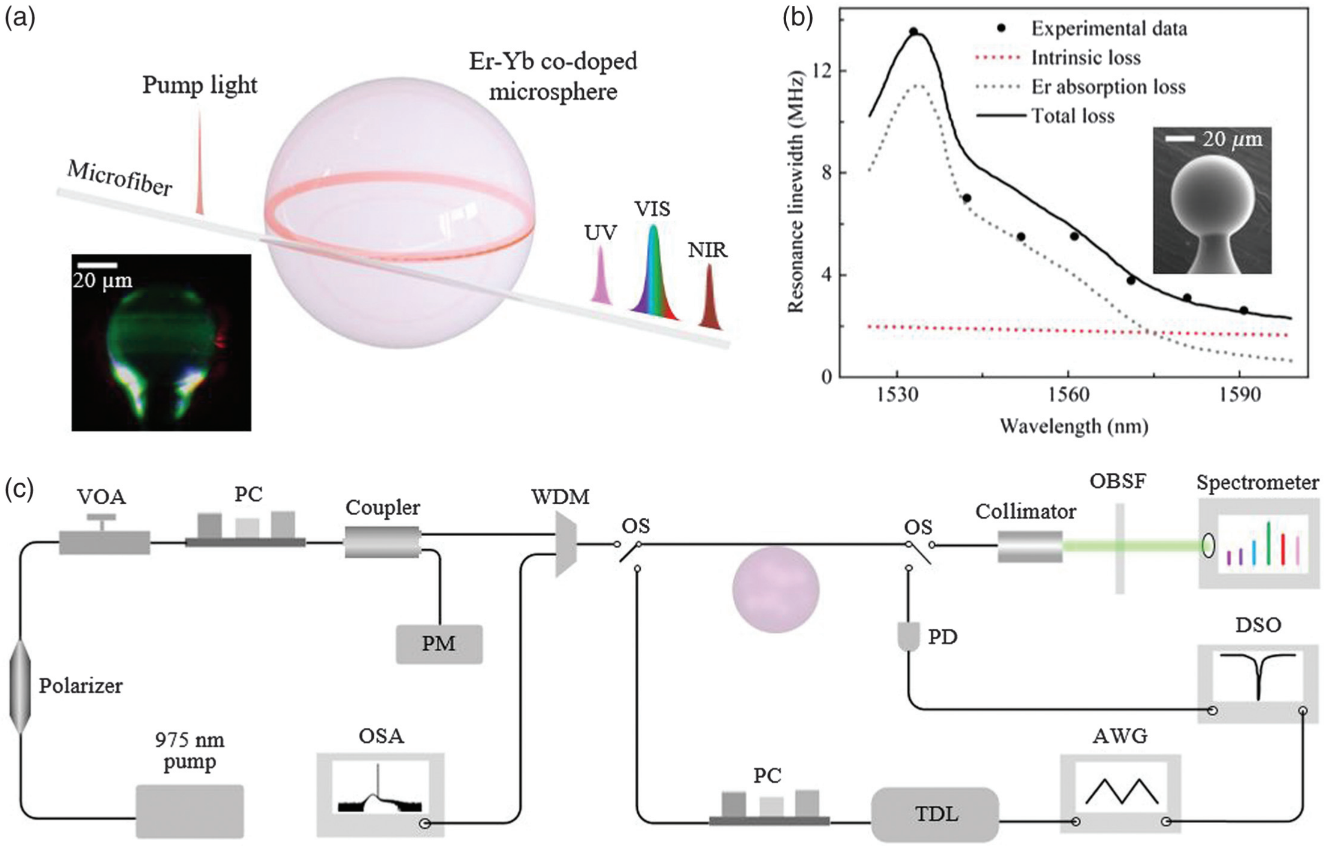

Fig. 1 Simultaneous ultraviolet, visible, and near-infrared CW lasing at room temperature. (a) Schematic of ultraviolet, visible, and near-infrared lasing by an Er-Yb co-doped microsphere under 975-nm CW laser excitation. Inset: Optical image of an Er-Yb co-doped microsphere with a diameter of 57 μm under a 4-mW pump. (b) Total optical loss evolution over six FSRs, including the theoretical Er-induced absorption loss and the intrinsic loss of the Er-Yb co-doped microsphere. Inset: Scanning electron microscopy image of the microsphere. (c) Experimental setup. VOA, variable optical attenuator; PM, power meter; PC, polarization controller; WDM, wavelength division multiplexer; OSA, optical spectrum analyzer; OS, optical switch; OBSF, 975-nm optical band-stop filter; DSO, digital storage oscilloscope; TDL, tunable diode laser; AWG, arbitrary waveform generator; PD, photodetector.

several resonant wavelengths. Only a small fraction of the pump power can be coupled into the cavity, thus this pump scheme is called a nonresonant pump. In contrast, for a resonant pump, most of the pump power can be coupled into the resonance modes and thus significantly enhanced, achieving extremely high energy density for a low lasing threshold and high pump efficiency.[27] However, the resonant pump requires a wavelength-fine-tunable narrow-linewidth laser source. The inset of Fig. 1(a) is a charge coupled device (CCD) image of the microlaser with a pump power of 4 mW in which green luminescence is dominant while red light is glimmering because of the weak response of our CCD (Apico industrial camera) at 665 nm. The bright rings can be recognized as high-order WGMs. The homogeneous bright rings distribute without obvious scattering bright spots induced by ion clusters, indicating the homogeneous RE-ion doping.

White-like light can be seen in the tail of the microsphere, which should be attributed to the blue, green, and red leaky modes. The Q factor of the microcavity plays an essential role for achieving a short-wavelength upconversion laser. The intrinsic Q factor of the doped silica microcavity is mainly limited by scattering loss, while scattering loss will extremely increase when the emission wavelength gets shorter. Therefore, a homogeneous RE ion doping method without introducing obvious ion clusters and defects is necessary. Figure 1(b) shows the total loss of a certain resonance mode over six free spectrum ranges (FSRs), which is fitted by the absorption loss for Er ions at telecommunication wavelengths combined with the cavity scattering loss.[37,38] The frequency detuning measurement is performed using a tunable diode laser (Toptica, CTL 1550) sweeping over the resonant modes. To reduce the thermal nonlinear effect of the microcavity and the saturated absorption of Er ions, the pump power is below 10 μW and the sweeping speed is 4.8 MHz/μs. The theoretical fitted intrinsic loss over six FSRs indicates an ultrahigh intrinsic Q factor of about 1.1×10^8 in the telecommunication band, which is the highest Q factor among the RE-doped microcavities, and is very critical for achieving ultralow-threshold short-wavelength upconversion lasers. Further transmission spectrum is also exhibited in Sec. S1 in the Supplementary Material, where a resonance linewidth of 1.53 MHz indicates a loaded Q factor exceeding 1.2×10^8. As the overlap integrals between the distribution of Er ions and the mode field are considered, the effective doping concentrations of Er and Yb ions could be estimated as 1.27×10^{17} and $3.175 \times 10^{17}\ \mathrm{cm}^{-3}$, respectively.

All the experimental measurements were performed at room temperature. The structural symmetry of the microsphere cavity makes its eigenmodes twofold degenerate. Two traveling-wave modes in the cavity propagate in the opposite directions (clockwise and counterclockwise) with the same resonant frequency and polarization state. As shown in Fig. 1(c), we measured the optical spectra of the clockwise light from 350 to 835 nm by a spectrometer (with the resolution of 0.33 nm). The counterclockwise light is coupled into an OSA (with the resolution of 0.06 nm) via a WDM, which is used for the 1080- and 1550-nm band lasing spectrum acquisition.

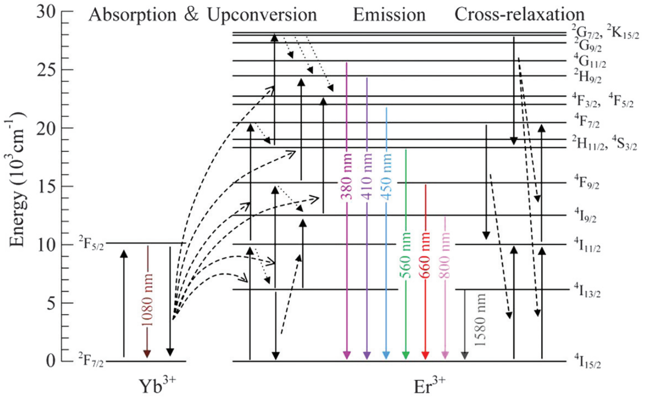

Fig. 2 Energy level diagram and proposed light emission mechanisms. The dashed and dotted arrows represent ET and multi-photon relaxation processes, respectively. The upward full arrows represent the upward transition induced by photon excitation or the ET process. The downward full arrows represent the downward transition induced by photon emission or the ET process.

3 Photoluminescence Analysis of the Er-Yb Co-Doped Silica Microcavity

A short-wavelength laser source can be realized by simultaneous two-photon and parametric oscillation processes. However, the parametric oscillation requires phase match, and simultaneous two-photon absorption requires ultrahigh energy density. In contrast, the upconversion processes in RE elements can be realized with their long-lived intermediate energy levels, which do not require phase match and ultrahigh energy density. As Er ions have abundant long-lived intermediate energy levels, manifold intraconfigurational transitions, and homogeneous energy levels distributions, they have the potential to realize ultraviolet upconversion lasers with 975-nm pumping. In general, the upconversion processes of RE elements are mainly contributed by excited state absorption (ESA), energy transfer (ET), photon avalanche (PA), and cooperative energy transfer processes.[39] Yb ions are used as the sensitizer to transfer energy to Er ions for improving upconversion luminescence.[40]

Figure 2 shows the emission mechanisms of the 380- ($^4G_{11/2} \rightarrow {}^4I_{15/2}$, ultraviolet light), 410- ($^2H_{9/2} \rightarrow {}^4I_{15/2}$, violet light), 450- ($^4F_{3/2}, {}^4F_{5/2} \rightarrow {}^4I_{15/2}$, blue light), 560- ($^4S_{3/2} \rightarrow {}^4I_{15/2}$, green light), 660- ($^4F_{9/2} \rightarrow {}^4I_{15/2}$, red light), 800- ($^4I_{9/2} \rightarrow {}^4I_{15/2}$, near-infrared light), 1080- ($^2F_{3/2} \rightarrow {}^2F_{5/2}$, near-infrared light), and 1550-nm ($^4I_{13/2} \rightarrow {}^4I_{15/2}$, near-infrared light) bands in which the 1080-nm photons are emitted by Yb ions while the others are emitted by Er ions. It is worth noting that both the $^2H_{11/2}$ and the $^4S_{3/2}$ states transit to the ground state will emit green photons. However, because these two energy levels have different lifetimes and populations, their lasing behaviors are different. In this work, the transition of $^4S_{3/2} \rightarrow {}^4I_{15/2}$ is the only consideration for green lasing. Under the 975-nm laser excitation, first, ground state absorption induces the transitions of $^2F_{7/2} \xrightarrow{\text{GSA}} {}^2F_{5/2}$ (Yb ions) and $^4I_{15/2} \xrightarrow{\text{GSA}} {}^4I_{11/2}$ (Er ions). Subsequently, a portion of the $^4I_{11/2}$ states transit to the $^4I_{13/2}$ states rapidly with phonon-assisted nonradiative relaxation (NR). Then, the ESA process in Er ions and the ET process from the excited Yb and Er ions to the adjacent excited Er ions will resonantly generate upward transitions. The main upconversion processes are provided as follows: $^4I_{11/2} \xrightarrow{\text{ESA/ET}} {}^4F_{7/2} \xrightarrow{\text{NR}} {}^4S_{3/2} \xrightarrow{\text{ESA/ET}} {}^2G_{7/2}$, $^2K_{15/2} \xrightarrow{\text{NR}} {}^4G_{11/2}$, $^2H_{9/2}$, $^4F_{3/2}, {}^4F_{5/2}$, $^4I_{13/2} \xrightarrow{\text{ET}} {}^4I_{9/2} \xrightarrow{\text{ESA/ET}} {}^4F_{3/2}, {}^4F_{5/2}$ (the transition of

$^4I_{13/2} \rightarrow {}^4I_{9/2}$ refers to the ET process between two Er ions of $^4I_{13/2}$), and $^4I_{13/2} \xrightarrow{\text{ESA/ET}} {}^4F_{9/2} \xrightarrow{\text{EAS/ET}} {}^2H_{9/2}$.

4 Lasing Characterization of the Er-Yb Co-Doped Microcavity

Considering that the mode spacing is proportional to square of the wavelength, the microsphere with the 57-μm diameter has a large number of resonance modes in short-wavelength bands. In this situation, the competition among the lasing modes is unpredictable, and the lasing modes cannot be clearly distinguished by the spectrometer, thus we characterize the emission intensity as the integration of the entire lasing band instead of the intensity of a certain lasing mode. Figure 3 shows the output intensity versus the pump power for the eight emission bands. At the low pump power, spontaneous emission intensity increases slowly at the beginning (corresponding to phase S_1). When the pump power reaches the lasing threshold, the slope of the curve will increase superlinearly (corresponding to phase S_2), exhibiting an abrupt change, and indicating the lasing onset. Further increasing the pump power, the slope of the curve will decrease (corresponding to phase S_3), as the emission intensity tends to be saturated. The entire curve exhibits a typical S-like behavior. The lasing thresholds are estimated through fitting the data dots by straight lines, and the crossover point of spontaneous emission and stimulated emission regions is defined as the lasing threshold.

Figure 3(a) shows the lasing thresholds of the 380- and 410-nm bands, which are about 480 and 170 μW, respectively. Such low-threshold CW upconversion lasing under room temperature indicates a feasible approach to obtain ultraviolet and violet lasing using mature near-infrared semiconductor lasers. It should be noted that, among the RE element-based lasers, the ultraviolet (380 nm) and violet (410 nm) CW upconversion lasing is first demonstrated under room temperature. The lasing thresholds of the 450- and 800-nm bands are estimated to be 2.7 and 1.7 μW, respectively, as shown in Fig. 3(b). The 450-nm CW upconversion lasing by the Er element is also first realized under room temperature. As the populations of the $^4F_{3/2}$ and $^4F_{5/2}$ are mainly provided by the transition of the $^4I_{9/2} \xrightarrow{\text{ESA/ET}} {}^4F_{3/2}, {}^4F_{5/2}$, their lasing curves are interdependent and similar. Figure 3(c) indicates that the lasing thresholds of the 560- and 660-nm

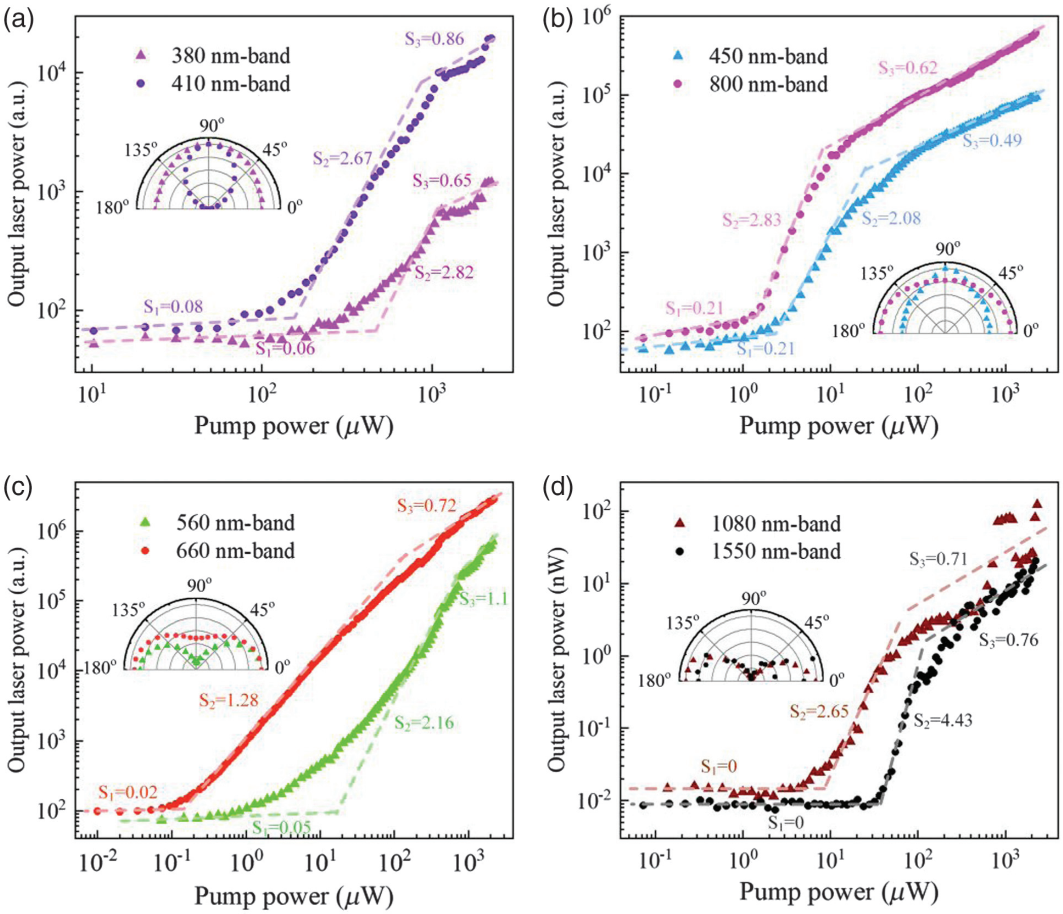

Fig. 3 Thresholds and polarization characteristics of ultraviolet, visible, and near-infrared CW lasing. The emission intensity versus the pump power in log–log scale, where *S* represents the slope. Inset: The emission intensity as a function of the polarization angle. The upconversion emission intensities are integrated from (a) 380 to 396 nm and 402 to 426 nm, (b) 450 to 489 nm and 756 to 816 nm, (c) 555 to 575 nm and 645 to 590 nm. (d) The downshifting emission intensities are summarized from the intensities of individual lasing wavelengths.

bands are 19 and 0.18 μW, respectively. The lasing threshold of the 560-nm band is lower than that obtained in the Er-doped silica microtoroid[34] and the Er-fluoride glass microsphere under the resonant pump.[41] An extraordinarily low lasing threshold of the 660-nm band is achieved, which is about 1/70th of that of the 560-nm band. This contrast is attributed to the difference between their intermediate energy level lifetimes during the upconversion processes. The lifetimes of the $^4I_{11/2}$ are much shorter than that of the $^4I_{15/2}$, which means that the population of the $^4S_{3/2}$ requires the higher pump power to be inverted. Figure 3(d) indicates that the lasing thresholds of the 1080- (emitted by Yb ions) and 1550-nm bands are about 10 and 38 μW, respectively. The lasing threshold of the 1550-nm band is lower than 1/50th of the reported lowest threshold under the nonresonant pump[42–44] and is close to those under the resonant pump.[30,40,44,45] In many cases, the thresholds of upconversion lasers are higher than those of downshifting lasers. However, in this case, the thresholds of the downshifting lasers are higher than those of the 450-, 660-, and 800-nm bands. The lasing threshold is mainly determined by the pump efficiency, gain material induced absorption loss, intrinsic cavity loss, and coupling loss. In our scheme, the 1080- and 1550-nm band lasing modes are overcoupled, resulting in high coupling losses and increases of the 1080- and 1550-nm band lasing thresholds. In contrast, the upconversion lasing modes are located at the weak coupling region. Given that the Er ion absorption loss is far larger than the intrinsic cavity loss at telecommunication wavelengths, the lifetimes of the upper states are much shorter than those of the $^4I_{15/2}$ states. As a result, inverting the populations to eliminate the gain material-induced absorption loss should be primarily considered for the upconversion lasing. Therefore, the upconversion lasing thresholds are highly dependent on the numbers of the absorbed photons and the lifetimes of the intermediate energy levels during the upconversion processes.

In our experiments, it is worth noting that the slopes of the pump-output curves will be lowered due to the intensive competition among the multiple lasing bands for limited excited populations (for detailed discussion, see Sec. S2 in the Supplementary Material). Furthermore, around the lasing thresholds, the pump-output curves exhibit gradual slope changes. This should be attributed to large spontaneous emission coupling factors (β). Spontaneous emission coupling factor is defined as the ratio of the emission band coupled into the WGMs: $\beta = F_p/(1+F_p)$,[46] where F_p represents the Purcell factor. The Purcell factor can be expressed as

$$F_p = \frac{3}{4\pi^2} \cdot \frac{(\lambda_0/n_{\mathrm{eff}})^3}{V_{\mathrm{eff}}} \cdot Q_{\mathrm{eff}},$$

where V_{eff} represents the effective mode volume, n_{eff} represents the mode effective refractive index, λ_0 represents the resonant wavelength, and Q_{eff} represents the quality factor of the system ($Q_{\mathrm{eff}}^{-1} = Q_w^{-1} + Q_e^{-1}$, where Q_w and Q_e represent the quality factors of the WGMs and the emitters, respectively).[47] As F_p is inversely proportional to V_{eff}, the enhanced spontaneous emission could occur in the microlaser.

The polarization state of the multiband microlaser is also examined. The insets show that the variations of the relative emission intensities by rotating the polarizer from 0 deg to 180 deg with a step size of 10 deg. It can be found that the relative emission intensities of all lasing bands are symmetric with respect to 90 deg, which indicates that they are polarized. Among them, the lasing of the 410-, 560-, 1080-, and 1550-nm bands is linearly polarized, and the lasing in the 380-, 450-, 660-, and 800-nm bands is elliptically polarized, which is because multiple lasing modes can comprise orthogonal polarized transverse electric (TE) and transverse magnetic (TM) modes.

To characterize the lasers in more detail, the lasing spectra under different pump powers are shown in Fig. 4. Under the 3-μW pump power excitation, the 660- and 800-nm bands have reached the lasing thresholds, as shown in Fig. 4(a). The peak around 488 nm is attributed to the $^4F_{7/2} \rightarrow {}^4I_{15/2}$ transition. A portion of the states of the $^4F_{7/2}$ will transit to the $^2H_{11/2}$ and the $^4S_{3/2}$ states, and then emit green photons, as shown in Fig. 2. Under the 36-μW pump power excitation, the 450-, 560-, and 1080-nm band lasers are achieved, as shown in Fig. 4(b). Interestingly, there are also several wide-linewidth peaks around 1535 nm, as shown in the inset of Fig. 4(b). However, according to Fig. 3(d), with this pump power below the lasing threshold, the 1550-nm band lasing has not been achieved. These wide-linewidth peaks are attributed to the Purcell-enhanced spontaneous emission. Owing to the Purcell effect, spontaneous emission will be enhanced, emerging some spontaneous emission peaks locating at the multiple adjacent resonance wavelengths of the cavity. However, the spacings of the adjacent peaks are too small to be resolved by the OSA with the resolution of 0.06 nm, and eventually some wide-linewidth peaks emerged. These spontaneous emission peaks can be easily distinguished with the laser peaks by their linewidths, which are about 0.8 and 0.06 nm, respectively. As shown in Fig. 4(c), under the pump power of 100 μW, lasing in the 1550-nm band has been achieved. Er ions have two gain peaks around 1535 and 1550 nm ($^4I_{13/2} \rightarrow {}^4I_{15/2}$). However, in this highly Er-doped scheme, under weak pumping, the reabsorption effect makes the device lase at 1564.56 nm first. With the higher pump power, the reabsorption effect weakens, and the laser peaks shift to the shorter wavelengths. As the pump power is increased to 1100 μW, the lasing in the 380- and 410-nm bands is also achieved, as shown in Fig. 4(d). The laser intensities of the 380- and 410-nm bands are relatively weak, compared with the other lasing bands. Except for the weaker intrinsic emission intensities, this is caused by weaker coupling strengths between the microsphere and the microfiber in the 380- and 410-nm bands, which leads to a small number of the emitted photons being coupled out and detected by the spectrometer (corresponding theoretical analysis is shown in Sec. S3 in the Supplementary Material). With the pump power increased from 100 to 1100 μW, the laser intensities of the 450-, 800-, and 1550-nm bands increase slightly, while the laser intensities of the 560- and 660-nm bands increase significantly. Under the increased pump power, plenty of the $^4I_{15/2}$ and the $^4I_{13/2}$ states transit to the upper energy levels; as the result, the densities of the $^4I_{9/2}$, the $^4F_{3/2}$, and the $^4F_{5/2}$ states are restrained, as they are positively related to the density of the $^4I_{15/2}$ state. The lasing mode spacings of the 380-, 410-, 450-, 560-, 660-, 800-, 1080-, and 1550-nm bands are about 0.56, 0.642, 0.8, 1.19, 1.70, 2.44, 4.6, and 9.6 nm, which are well matched with the calculated FSRs of 0.56, 0.65, 0.82, 1.22, 1.72, 2.53, 4.72, and 9.83 nm, respectively. The FSR is calculated by FSR $= \lambda_0^2/\pi D n_g$, where λ_0 represents the center wavelength of the WGMs, D represents the diameter of the cavity, and n_g represents the group refractive index. Here, the refractive index of doped silica is set to the

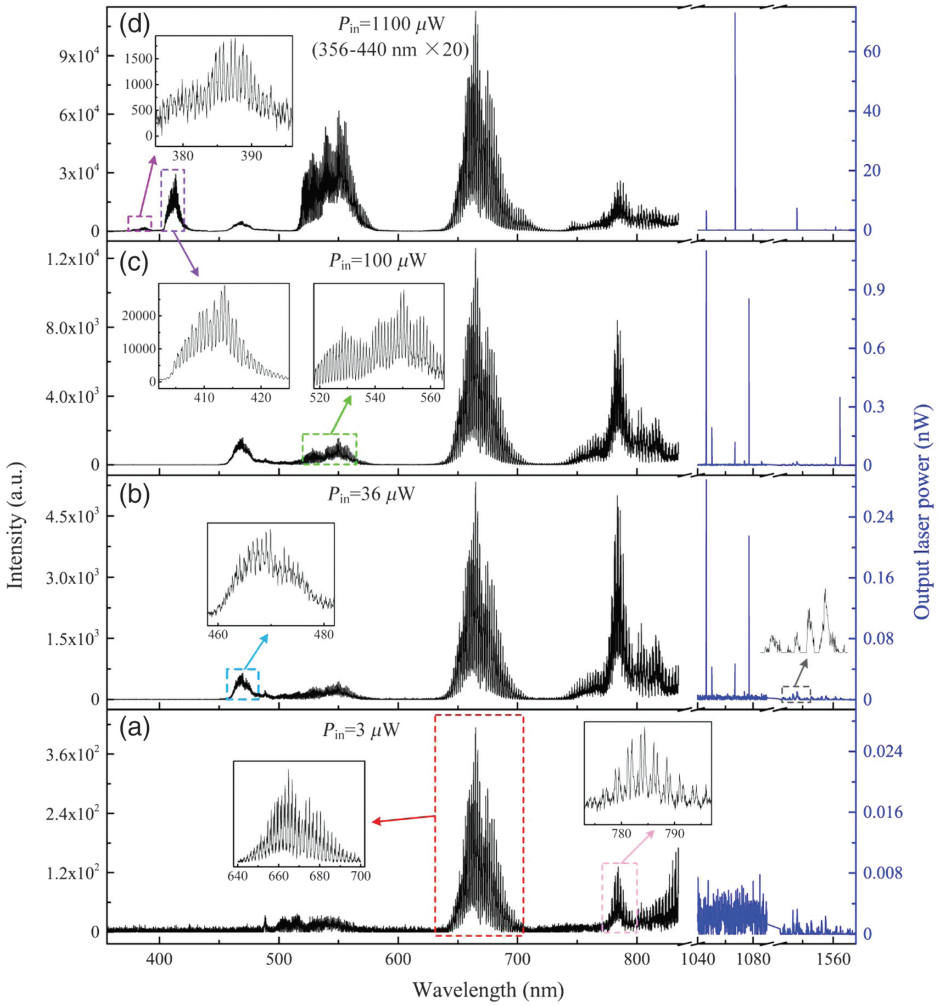

Fig. 4 Lasing spectrum evolution with the increased pump power. The lasing spectra (black line) from 350 to 835 nm are acquired by the spectrometer. The lasing spectra (blue line) from 1040 to 1090 nm and 1525 to 1590 nm are acquired by the OSA. The pump powers are (a) 3, (b) 36, (c) 100, and (d) 1100 μW, respectively, from the bottom to the top. The insets are the zoom-in lasing spectra.

same as that of pure silica for the calculation, which should bring a permissible deviation.[48]

One of the characteristics of the lasing onsets is distinct spectral linewidth narrowing around the lasing threshold. However, in our scheme, the linewidths of the lasers and the Purcell enhanced spontaneous emission peaks are too narrow to be resolved by the spectrometer. Despite this fact, the mode-competition-induced evolutions of the lasing spectra can still be used to confirm the lasing onsets (for details, see Sec. S4 in the Supplementary Material).

Compared with downshifting lasing, upconversion lasing usually requires a higher energy density. However, high pump intensity may cause thermal and optical damages for gain materials, which leads to the failure of laser emission or the lasing wavelength drifting. Previous works about RE-based upconversion lasers usually employed a pulsed laser pump or a cryogenic environment to avoid thermal damage. For our CW lasing under room temperature, we test their stabilities by measuring the variations of the lasing intensities and the lasing wavelengths over 190 min. As shown in Fig. 5(a), the lasing in the 380- and 410-nm bands exhibits a great lasing intensity stability, with small degradations (5.7% and 3.8%, respectively) and standard deviations (3.3% and 2%, respectively) of the intensity. The lasing intensities of the 450-, 800-, and 1080-nm bands degraded at the beginning and then stabilized. In contrast, the lasing intensities of the 560-, 660-, and 1550-nm bands increased slightly at the beginning and then stabilized. As shown in the Fig. 5(b), the maximum wavelength drifts for the 450-, 600-, and 800-nm bands are 0.452, 0.47, and 0.9 nm, respectively, which correspond to one or two pixel sizes of the spectrometer. This result indicates the good lasing intensity stability and excellent lasing wavelength stability of the microlaser, making it possible for practical applications.

5 Conclusion

We have proposed and demonstrated a simple and effective method for homogeneously doping RE elements into a silica microcavity. Through this method, we fabricated a 57-μm-diameter Er-Yb co-doped silica microsphere with the highest

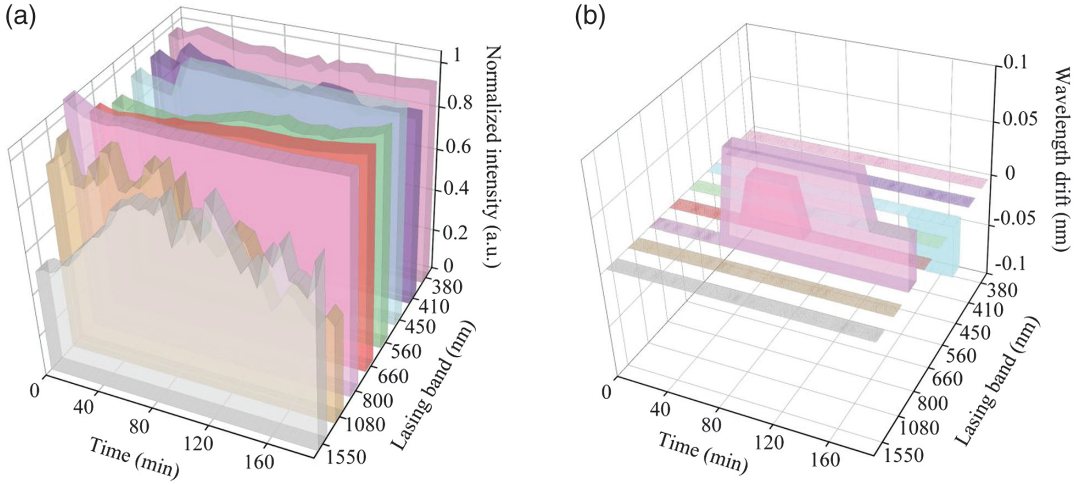

Fig. 5 Lasing stability. (a) Lasing intensity and (b) wavelength evolution over the duration of 190 min, exhibiting stable emission intensities and slight wavelength drifts.

intrinsic Q factor among the RE-doped microcavities up to 1.1×10^8 in the telecommunication band, achieving simultaneous ultraviolet, visible, and near-infrared CW lasing under room temperature with submilliwatt-level thresholds. This multiband microlaser exhibits a good emission intensity stability and an excellent wavelength stability over 190 min. The significance of this demonstration can be understood in several aspects. First, simultaneous ultraviolet, visible, and near-infrared lasing has been achieved by an individual microcavity, of which lasing over a wavelength range of 1170 nm by a single gain material (Er element) has been realized. Among them, stable ultraviolet and violet upconversion lasing by RE elements is first realized under room temperature and a CW pump. Second, benefitting from the ultrahigh Q factor of the doped microcavity, the multiband microlaser has narrow linewidths and ultralow thresholds, exhibiting extraordinary lasing performances. Third, the desired lasers can be obtained by different RE elements via upconversion or downshifting processes, which allows for flexible pump schemes and abundant lasing wavelengths. Besides these advantages in laser application, this ultrahigh-Q doped microcavity is also an excellent platform for ultrahigh-precision sensing, optical memories, and cavity–matter–light interaction investigations.

Acknowledgments

This work was supported by the National Natural Science Foundation of China (91850115, 11774110), the Fundamental Research Funds for the Central Universities (HUST: 2019kfyXKJC036, 2019kfyRCPY092), the State Key Laboratory of Advanced Optical Communication Systems and Networks (2021GZKF003), and the State Key Laboratory of Applied Optics (SKLAO2021001A10).

References

1. F. Fan et al., “A monolithic white laser,” *Nat. Nanotechnol.* **10**(9), 796–803 (2015).
2. C. Zhang et al., “Dual-color single-mode lasing in axially coupled organic nanowire resonators,” *Sci. Adv.* **3**(7), e1700225 (2017).
3. Z. Liu et al., “Dynamical color-controllable lasing with extremely wide tuning range from red to green in a single alloy nanowire using nanoscale manipulation,” *Nano Lett.* **13**(10), 4945–4950 (2013).
4. J. Xu et al., “Room-temperature dual-wavelength lasing from single-nanoribbon lateral heterostructures,” *J. Am. Chem. Soc.* **134**(30), 12394–12397 (2012).
5. Y. Lu et al., “Tunable lifetime multiplexing using luminescent nanocrystals,” *Nat. Photonics* **8**(1), 32–36 (2014).
6. H. H. Gorris and O. S. Wolfbeis, “Photon-upconverting nanoparticles for optical encoding and multiplexing of cells, biomolecules, and microspheres,” *Angew. Chem. Int. Ed. Engl.* **52**(13), 3584–3600 (2013).
7. R. Deng et al., “Temporal full-colour tuning through non-steady-state upconversion,” *Nat. Nanotechnol.* **10**(3), 237–242 (2015).
8. F. Wang et al., “Simultaneous phase and size control of upconversion nanocrystals through lanthanide doping,” *Nature* **463**(7284), 1061–1065 (2010).
9. H. A. Höppe, “Recent developments in the field of inorganic phosphors,” *Angew. Chem. Int. Ed.* **48**(20), 3572–3582 (2009).
10. F. Wang et al., “Tuning upconversion through energy migration in core-shell nanoparticles,” *Nat. Mater.* **10**(12), 968–973 (2011).
11. B. Zhou et al., “Controlling upconversion nanocrystals for emerging applications,” *Nat. Nanotechnol.* **10**(11), 924–936 (2015).
12. Z. Chen et al., “Emerging and perspectives in microlasers based on rare-earth ions activated micro-/nanomaterials,” *Prog. Mater. Sci.* **121**, 100814 (2021).
13. A. Godard, “Infrared (2–12 μm) solid-state laser sources: a review,” *C. R. Phys.* **8**(10), 1100–1128 (2007).
14. F. Vollmer and S. Arnold, “Whispering-gallery-mode biosensing: label-free detection down to single molecules,” *Nat. Methods* **5**(7), 591–596 (2008).
15. Y. Zhi et al., “Single nanoparticle detection using optical microcavities,” *Adv. Mater.* **29**(12), 1604920 (2017).
16. K. D. Heylman et al., “Optical microresonators for sensing and transduction: a materials perspective,” *Adv. Mater.* **29**(30), 1700037 (2017).
17. T. J. Kippenberg et al., “Dissipative kerr solitons in optical microresonators,” *Science* **361**(6402), eaan8083 (2018).
18. T. J. Kippenberg, S. M. Spillane, and K. J. Vahala, “Kerr-nonlinearity optical parametric oscillation in an ultrahigh-Q toroid microcavity,” *Phys. Rev. Lett.* **93**(8), 083904 (2004).
19. X. Shen et al., “Raman laser from an optical resonator with a grafted single-molecule monolayer,” *Nat. Photonics* **14**(2), 95–101 (2020).
20. X. Zhang et al., “Symmetry-breaking-induced nonlinear optics at a microcavity surface,” *Nat. Photonics* **13**(1), 21–24 (2019).

21. J.-H. Chen et al., "Microcavity nonlinear optics with an organically functionalized surface," *Phys. Rev. Lett.* **123**(17), 173902 (2019).
22. W. Wang, L. Wang, and W. Zhang, "Advances in soliton microcomb generation," *Adv. Photonics* **2**(3), 034001 (2020).
23. Z. Shen et al., "Experimental realization of optomechanically induced non-reciprocity," *Nat. Photonics* **10**(10), 657–661 (2016).
24. M. Aspelmeyer, T. J. Kippenberg, and F. Marquardt, "Cavity optomechanics," *Rev. Mod. Phys.* **86**(4), 1391–1452 (2014).
25. K. J. Vahala, "Optical microcavities," *Nature* **424**(6950), 839–846 (2003).
26. J. Yang et al., "Multiphysical sensing of light, sound and microwave in a microcavity Brillouin laser," *Nanophotonics* **9**(9), 2915–2925 (2020).
27. L. He, Ş. K. Özdemir, and L. Yang, "Whispering gallery microcavity lasers," *Laser Photonics Rev.* **7**(1), 60–82 (2013).
28. S. Yang, Y. Wang, and H. Sun, "Advances and prospects for whispering gallery mode microcavities," *Adv. Opt. Mater.* **3**(9), 1136–1162 (2015).
29. O. Salehzadeh et al., "Optically pumped two-dimensional MoS_2 lasers operating at room-temperature," *Nano Lett.* **15**(8), 5302–5306 (2015).
30. T. J. Kippenberg et al., "Demonstration of an erbium-doped microdisk laser on a silicon chip," *Phys. Rev. A* **74**(5), 051802 (2006).
31. L. Yang et al., "Erbium-doped and raman microlasers on a silicon chip fabricated by the sol-gel process," *Appl. Phys. Lett.* **86**(9), 091114 (2005).
32. S. Mehrabani and A. M. Armani, "Blue upconversion laser based on thulium-doped silica microcavity," *Opt. Lett.* **38**(21), 4346–4349 (2013).
33. X.-F. Jiang et al., "Whispering-gallery microcavities with unidirectional laser emission," *Laser Photonics Rev.* **10**(1), 40–61 (2016).
34. T. Lu et al., "On-chip green silica upconversion microlaser," *Opt. Lett.* **34**(4), 482–484 (2009).
35. A. Fernandez-Bravo et al., "Ultralow-threshold, continuous-wave upconverting lasing from subwavelength plasmons," *Nat. Mater.* **18**(11), 1172–1176 (2019).
36. H. Zhu et al., "Amplified spontaneous emission and lasing from lanthanide-doped up-conversion nanocrystals," *ACS Nano* **7**(12), 11420–11426 (2013).
37. W. L. Barnes et al., "Absorption and emission cross section of Er^{3+} doped silica fibers," *IEEE J. Quantum Electron.* **27**(4), 1004–1010 (1991).
38. M. L. Gorodetsky, A. A. Savchenkov, and V. S. Ilchenko, "Ultimate Q of optical microsphere resonators," *Opt. Lett.* **21**(7), 453–455 (1996).
39. L.-D. Sun et al., "Upconversion of rare earth nanomaterials," *Annu. Rev. Phys. Chem.* **66**(1), 619–642 (2015).
40. H.-S. Hsu, C. Cai, and A. M. Armani, "Ultra-low-threshold Er:Yb sol-gel microlaser on silicon," *Opt. Express* **17**(25), 23265–23271 (2009).
41. W. V. Klitzing et al., "Very low threshold green lasing in microspheres by up-conversion of IR photons," *J. Opt. B Quantum Semiclass. Opt.* **2**(2), 204–206 (2000).
42. S. Zhu et al., "All-optical tunable microlaser based on an ultra-high-Q erbium-doped hybrid microbottle cavity," *ACS Photonics* **5**(9), 3794–3800 (2018).
43. J. M. Ward, Y. Yang, and S. Nic Chormaic, "Glass-on-glass fabrication of bottle-shaped tunable microlasers and their applications," *Sci. Rep.* **6**, 25152 (2016).
44. Y. Yang et al., "Tunable erbium-doped microbubble laser fabricated by sol-gel coating," *Opt. Express* **25**(2), 1308–1313 (2017).
45. L. Yang, D. K. Armani, and K. J. Vahala, "Fiber-coupled erbium microlasers on a chip," *Appl. Phys. Lett.* **83**(5), 825–826 (2003).
46. A. Jeantet et al., "Widely tunable single-photon source from a carbon nanotube in the purcell regime," *Phys. Rev. Lett.* **116**(24), 247402 (2016).
47. C. Javerzac-Galy et al., "Excitonic emission of monolayer semiconductors near-field coupled to high-Q microresonators," *Nano Lett.* **18**(5), 3138 (2018).
48. S. Abedrabb et al., "Optical polarizability of erbium-oxygen complexes in sol-gel-based silica films," *J. Phys. D Appl. Phys.* **54**(13), 135101 (2021).
49. L. He et al., "Detecting single viruses and nanoparticles using whispering gallery microlasers," *Nat. Nanotechnol.* **6**(7), 428–432 (2011).
50. D. G. O. Shea et al., "An all-fiber coupled multicolor microspherical light source," *IEEE Photonics Technol. Lett.* **19**(21), 1720–1722 (2007).
51. C.-L. Zou et al., "Taper-microsphere coupling with numerical calculation of coupled-mode theory," *J. Opt. Soc. Am. B* **25**(11), 1895–1898 (2008).
52. Y. Liang et al., "Competition of whispering gallery lasing modes in microwire with hexagonal cavity," *J. Phys. D Appl. Phys.* **54**(5), 055107 (2020).
53. X. Chen et al., "Confining energy migration in upconversion nanoparticles towards deep ultraviolet lasing," *Nat. Commun.* **7**(1), 10304 (2016).
54. X. Chen et al., "Energy migration upconversion in Ce(III)-doped heterogeneous core-shell-shell nanoparticles," *Small* **13**(43), 1701479 (2017).
55. T. Wang et al., "White-light whispering-gallery-mode lasing from lanthanide-doped upconversion $NaYF_4$ hexagonal microrods," *ACS Photonics* **4**(6), 1539–1543 (2017).
56. A. Fernandez-Bravo et al., "Continuous-wave upconverting nanoparticle microlasers," *Nat. Nanotechnol.* **13**(7), 572–577 (2018).
57. Y. Liu et al., "Controlled assembly of upconverting nanoparticles for low-threshold microlasers and their imaging in scattering media," *ACS Nano* **14**(2), 1508–1519 (2020).
58. Y. Shang et al., "Low threshold lasing emissions from a single upconversion nanocrystal," *Nat. Commun.* **11**, 6156 (2020).
59. T. Sun et al., "Ultralarge anti-Stokes lasing through tandem upconversion," *Nat. Commun.* **13**, 1032 (2022).

Biographies of the authors are not available.